ELSEVIER

A periodic FMM for Maxwell's equations in 3D and its applications to problems related to photonic crystals

Yoshihiro Otani, Naoshi Nishimura *

*Department of Applied Analysis and Complex Dynamical Systems, Graduate School of Informatics, Kyoto University,
Kyoto 606-8501, Japan*

Abstract

This paper presents an FMM (Fast Multipole Method) for periodic boundary value problems for Maxwell's equations in 3D. The effect of periodicity is taken into account with the help of the periodised moment to local expansion (M2L) transformation formula, which includes lattice sums. We verify the proposed method by comparing the obtained numerical results with analytic solutions for models of the multi-layered dielectric slab. We then apply the proposed method to scattering problems for periodic two-dimensional arrays of dielectric spheres and compare the obtained energy transmittances with those from the previous studies. We also consider scattering problems for woodpile crystals, where we find a passband related to a localised mode. Through these numerical tests we conclude that the proposed method is efficient and accurate.
© 2008 Elsevier Inc. All rights reserved.

Keywords: BIEM; FMM; Periodic problems; Maxwell's equations; Photonic crystals

1. Introduction

Solving periodic boundary value problems for wave problems has been one of important subjects in science and engineering because there are many applications which are formulated into problems of this type. This has been particularly true in the field of electromagnetics, where periodicity plays important roles in the design of gratings, wave guides, etc. Due to the development of nanotechnology, the importance of periodic boundary value problems is further increased. For example, it is now possible to produce periodic structures called 'photonic crystals' which are composed of dielectric materials having a geometric periodicity comparable to the wavelength of light [1]. Because of this periodicity, photonic crystals show various interesting behaviours. For example, photonic crystals enable us to control light freely since they provide means to guide or store it. In addition, one can design photonic crystals in a way that they prohibit the propagation of waves in a

certain frequency range called the stopband. One can also make a small passband within the stopband by introducing a small defect in the periodic structure, which will produce a localised mode near the defect. Other research and development activities include zero threshold lasers, large scale optical integrated circuit etc., which would have been impossible only with conventional technologies. Photonic crystals are thus expected to revolutionise the optical technology in the future. Also noteworthy is another emerging technology called metamaterials [2]. Metamaterials are a class of composite materials, which usually have subwavelength periodic structures. Metamaterials exhibit curious behaviours which no natural materials possess. Particularly interesting are the so called 'left handed metamaterials', which are said to have negative apparent refractive indices. With left-handed metamaterials it will be possible to produce the so called 'super lens' having a very high resolution which no materials with positive refractive indices can achieve. Typical left-handed metamaterials have periodic structures composed of dielectric matrices (including air) with nano-scale metallic inclusions.

For the analysis of the optical fields within periodic structures, it is customary to use numerical techniques such as FDTD methods, FEM, BIEM (also called BEM or Method of Moments), and the methods of the plane wave expansion, etc. As far as one is mainly interested in understanding fundamental properties of periodic structures, it may be sufficient to deal with relatively simple models with these numerical methods. If one considers models with more complicated geometries, as will be the case when one is interested in industrial applications, one will have to solve large scale problems. Boundary Integral Equation Methods (BIEM) have potential as solvers for large problems because of their boundary only nature. This is particularly true when the problem is related to scattering since BIEM can deal with radiation conditions in a natural manner. Although the $O(N^2)$ (N is the number of unknowns) complexity of BIEM has been a serious problem in applying this method to large problems, the rapid development of the fast BIEMs including the acceleration with Fast Multipole Methods (FMM) [3,4] has ameliorated the situation considerably in these decades.

However, the investigations of the fast multipole accelerated BIEMs have so far been directed mainly to standard problems of the benchmark type where one seeks to solve larger problems faster using relatively simple model problems. Although some of recent investigations consider applications of this method to real world problems, we still see little applications of FMMs to periodic wave problems in 3D in spite of their important applications in science and engineering. In view of this, the present investigation aims at formulating and testing a periodic FMM for Maxwell's equations in 3D.

As a matter of fact, the basic idea of using FMMs in periodic boundary value problems has been presented in Greengard and Rokhlin [3], where they consider an infinite array of replicas of the unit cell in Laplace's equation in 2D. Their approach, however, is not without mathematical ambiguity since they evaluated a divergent series using a physical argument, and its extension to dynamics is not straightforward. Otani and Nishimura presented mathematically sound formulations for elastostatics in 2D [5] and in 3D [6] and demonstrated their numerical performances. For wave problems, Otani and Nishimura considered Helmholtz' equations in 2D [7]. To the best of the knowledge of the present authors, however, not much has been done in similar problems in 3D, except in a conference paper by Yeung and Barouch [8]. These authors use multipole expansions around points which are not at the centre of replicas of the unit cell in order to improve the convergence of lattice sums. But, this approach will not necessarily be efficient because the proposed change of the centres of expansions will increase the required number of multipoles for a given accuracy.

In the present investigation we deal with two periodic boundary value problems for Maxwell's equations in 3D, where we impose periodic boundary conditions only in two directions in the three-dimensional space. The periodicity is introduced with the help of the periodic Green's function. The solution of the resulting integral equation is accelerated with the periodic FMM which considers an infinite array of the replicas of the unit cell. In evaluating the effects of these replicas we use lattice sums of multipoles which are computed in the forms of Fourier integrals. After discussing the algorithm, we verify our approach by solving scattering problems for dielectric slabs where analytical solutions are available. Our approach is then applied to scattering problems for two-dimensional array of dielectric spheres and for woodpile structures, both of which are standard and important models in the field of photonic crystals. In the latter problem we find a passband related to a localised mode. Through these numerical tests we conclude efficiency and high accuracy of the proposed approach.

2. Formulation

In this paper, we shall use standard diadic and index notations for vectors and tensors and the summation convention for repeated indices. Also, the position vector of a point x will be denoted by either $\boldsymbol{x}$ or $\overrightarrow{Ox}$.

2.1. Non-periodic formulations in $\mathbb{R}^3$

We first consider the scattering problem for Maxwell's equations in 3D without imposing periodic boundary conditions. The reader is referred to Nédélec [9] for the integral representations of the solutions for Maxwell's equations.

2.1.1. Statement of the problem

We consider the whole space, $\mathbb{R}^3$, which is subdivided into N subdomains as shown in Fig. 1. Namely, we have $\mathbb{R}^3 = \overline{D_1 \cup D_2 \cup \cdots \cup D_N}$, $D_i \cap D_j = \phi$ $(i \neq j)$. In each of the subdomains D_i we assume that the following Maxwell's equations are satisfied:

$$\nabla \times \boldsymbol{E} = i\omega\mu^i \boldsymbol{H} \quad \text{in } D_i, \tag{1}$$

$$\nabla \times \boldsymbol{H} = -i\omega\epsilon^i \boldsymbol{E} \quad \text{in } D_i, \tag{2}$$

where ω is the frequency (with $e^{-i\omega t}$ time dependence), ϵ^i and μ^i are the dielectric constant and the magnetic permeability for the material occupying D_i. In addition, we assume that there exists one and only one infinite subdomain denoted by D_I.

As the boundary (interface) conditions we have the following: For a point $x^0 \in S_{ab}$ $(S_{ab} := \partial D_a \cap \partial D_b, a \neq b)$ we require

$$\lim_{x^a \to x^0} \boldsymbol{E}(x^a) \cdot \boldsymbol{T}(x^0) = \lim_{x^b \to x^0} \boldsymbol{E}(x^b) \cdot \boldsymbol{T}(x^0), \tag{3}$$

$$\lim_{x^a \to x^0} \boldsymbol{H}(x^a) \cdot \boldsymbol{T}(x^0) = \lim_{x^b \to x^0} \boldsymbol{H}(x^b) \cdot \boldsymbol{T}(x^0), \tag{4}$$

where $\boldsymbol{T}$ is an arbitrary vector tangential to S_{ab} at x^0, and $\lim_{x^a \to x^0}$ indicates the limit from within D_a, etc.

In addition, we assume that there exists an incident wave denoted by $(\boldsymbol{E}^{\text{inc}}, \boldsymbol{H}^{\text{inc}})$ in D_I, with which the scattered waves, denoted by the superscript $^{\text{sca}}$, are defined by $\boldsymbol{E}^{\text{sca}} = \boldsymbol{E} - \boldsymbol{E}^{\text{inc}}$ and $\boldsymbol{H}^{\text{sca}} = \boldsymbol{H} - \boldsymbol{H}^{\text{inc}}$. For the scattered waves we require the radiation conditions given as

$$\left| \sqrt{\epsilon^I} \boldsymbol{E}^{\text{sca}} - \sqrt{\mu^I} \boldsymbol{H}^{\text{sca}} \times \frac{\boldsymbol{x}}{|\boldsymbol{x}|} \right| \leqslant \frac{C}{|\boldsymbol{x}|^2},$$

$$\left| \sqrt{\epsilon^I} \boldsymbol{E}^{\text{sca}} \times \frac{\boldsymbol{x}}{|\boldsymbol{x}|} + \sqrt{\mu^I} \boldsymbol{H}^{\text{sca}} \right| \leqslant \frac{C}{|\boldsymbol{x}|^2}$$

as $|\boldsymbol{x}| \to \infty$, where C is a constant.
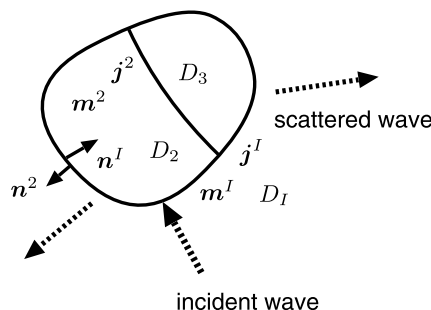

Fig. 1. Scattering problem in the whole space.

2.1.2. Boundary integral equations

The fundamental solutions Γ_{ip} for Maxwell's equations in 3D which satisfy

$$e_{ijk}e_{klm}\Gamma_{mp,lj}(\boldsymbol{x}) - k^2\Gamma_{ip}(\boldsymbol{x}) = \delta_{ip}\delta(\boldsymbol{x})$$

are well-known to have the following form:

$$\Gamma_{ip} = \left(\frac{1}{k^2}\frac{\partial}{\partial x_i}\frac{\partial}{\partial x_p} + \delta_{ip}\right)G,$$

where k is the wave number defined by $k = \omega\sqrt{\epsilon\mu}$, δ_{ij} is Kronecker's delta, e_{ijk} is the permutation symbol and $\delta(\boldsymbol{x})$ is Dirac's delta. Also, G is the fundamental solution for Helmholtz' equation in 3D given as follows:

$$G(\boldsymbol{x} - \boldsymbol{y}) = \frac{e^{ik|\boldsymbol{x}-\boldsymbol{y}|}}{4\pi|\boldsymbol{x} - \boldsymbol{y}|}.$$

One may also write Γ_{ip} in the following form modulo Dirac's delta:

$$\Gamma_{ip} = \frac{1}{k^2}e_{ijk}\frac{\partial}{\partial x_j}e_{pqk}\frac{\partial}{\partial y_q}G(\boldsymbol{x} - \boldsymbol{y}).$$

By substituting the fundamental solution into the Green formula we obtain the following integral representations for $\boldsymbol{E}$ and $\boldsymbol{H}$ for $x \in D_i$:

$$\boldsymbol{E}(x) = \delta_{iI}\boldsymbol{E}^{\mathrm{inc}}(x) + \int_{\partial D_i}\left(\boldsymbol{m}^i \times (\nabla_y G_i) - i\omega\mu^i\boldsymbol{j}^i G_i + \frac{i}{\omega\epsilon^i}\nabla_y G_i \mathrm{div}_S\boldsymbol{j}^i\right)\mathrm{d}S_y, \tag{5}$$

$$\boldsymbol{H}(x) = \delta_{iI}\boldsymbol{H}^{\mathrm{inc}}(x) + \int_{\partial D_i}\left(-\boldsymbol{j}^i \times (\nabla_y G_i) - i\omega\epsilon^i\boldsymbol{m}^i G_i + \frac{i}{\omega\mu^i}\nabla_y G_i \mathrm{div}_S\boldsymbol{m}^i\right)\mathrm{d}S_y, \tag{6}$$

where the subscript to G indicates the subdomain number. In this formula, $\boldsymbol{j}^i$ and $\boldsymbol{m}^i$, respectively, are the surface electric and magnetic current vectors for D_i defined by

$$\boldsymbol{j}^i(y) = \boldsymbol{n}^i(y) \times \boldsymbol{H}(y), \qquad \boldsymbol{m}^i(y) = \boldsymbol{E}(y) \times \boldsymbol{n}^i(y),$$

where $\boldsymbol{n}^i$ stands for the outward unit normal vector on the surface of the domain D_i, and div_S indicates the surface divergence defined by:

$$\mathrm{div}_S \phi = -(\nabla \times (\phi \times \boldsymbol{n})) \cdot \boldsymbol{n}.$$

One obtains the following variational boundary integral equations [9] as one uses (5), (6) and the boundary conditions given by (3) and (4):

$$0 = \sum_d \left(\delta_{dI}\int_{\partial D_d}\boldsymbol{t}^d(x) \cdot \boldsymbol{E}^{\mathrm{inc}}(x)\,\mathrm{d}S_x + \int_{\partial D_d}\int_{\partial D_d}\left\{\boldsymbol{t}^d(x) \cdot (\boldsymbol{m}^d(y) \times \nabla_y G_d(\boldsymbol{x} - \boldsymbol{y}))\right.\right.$$
$$\left.\left. -i\omega\mu^d\boldsymbol{t}^d(x) \cdot \boldsymbol{j}^d(y)G_d(\boldsymbol{x} - \boldsymbol{y}) + \frac{i}{\omega\epsilon^d}\mathrm{div}_S\boldsymbol{t}^d(x)\,\mathrm{div}_S\boldsymbol{j}^d(y)G_d(\boldsymbol{x} - \boldsymbol{y})\right\}\mathrm{d}S_y\,\mathrm{d}S_x\right), \tag{7}$$

$$0 = \sum_d \left(\delta_{dI}\int_{\partial D_d}\boldsymbol{t}^d(x) \cdot \boldsymbol{H}^{\mathrm{inc}}(x)\,\mathrm{d}S_x + \int_{\partial D_d}\int_{\partial D_d}\left\{-\boldsymbol{t}^d(x) \cdot (\boldsymbol{j}^d(y) \times \nabla_y G_d(\boldsymbol{x} - \boldsymbol{y}))\right.\right.$$
$$\left.\left. -i\omega\epsilon^d\boldsymbol{t}^d(x) \cdot \boldsymbol{m}^d(y)G_d(\boldsymbol{x} - \boldsymbol{y}) + \frac{i}{\omega\mu^d}\mathrm{div}_S\boldsymbol{t}^d(x)\,\mathrm{div}_S\boldsymbol{m}^d(y)G_d(\boldsymbol{x} - \boldsymbol{y})\right\}\mathrm{d}S_y\,\mathrm{d}S_x\right) \tag{8}$$

where

$$\boldsymbol{t}^d = \boldsymbol{T}' \times \boldsymbol{n}^d \tag{9}$$

and $\boldsymbol{T}'$ is a test function which is a tangent vector field on $S := \bigcup_d\partial D_d$. The tangential component of $\boldsymbol{T}'$ is assumed to be continuous across possible curves of discontinuity on S. The sums in (7) and (8) are on subdomains whose boundaries have non-void intersections with the support of $\boldsymbol{T}'$. Hence, these sums include a and b when the support of $\boldsymbol{T}'$ is included in S_{ab} to test the continuity condition between D_a and D_b. Note that these

equations are valid also at points where more than two subdomains meet. Also, note that (7) and (8) have no irregular frequencies since they are nothing other than the variational statements for the so called PMCHW(T) formulation [10], which is known to have unique solutions.

2.1.3. Fast multipole methods

This section collects formulae required in the fast multipole methods for Maxwell's equations for the purpose of referential convenience. The reader is referred to Chew et al. [10] for the details, although the formulation used in this paper is not identical with the one used by Chew et al.

In FMM for wave problems in frequency domain, we use two types of expansions of the fundamental solution. Namely,

- FMM based on the series expansion of the fundamental solution (low frequency FMM).
- FMM based on the diagonal form [11].

In this paper we follow Otani and Nishimura [12] to switch between these formulations depending on the level in the tree structure used in FMM, as we shall see in Section 3. This approach is introduced in order to control the accuracy of FMM. See also Jiang and Chew [13] and Cheng et al. [14] for related approaches.

We first present the low frequency FMM. To this end, we prepare the multipole expansions for the fundamental solution G for Helmholtz' equation in 3D in the following form:

$$G(\boldsymbol{x} - \boldsymbol{y}) = \frac{e^{ik|\boldsymbol{x}-\boldsymbol{y}|}}{4\pi|\boldsymbol{x}-\boldsymbol{y}|} = \frac{ik}{4\pi} \sum_{n=0}^{\infty} \sum_{m=-n}^{n} (2n+1)\widetilde{I}_n^m(\overrightarrow{Oy})O_n^m(\overrightarrow{Ox}), \tag{10}$$

where we have assumed $|\overrightarrow{Ox}| > |\overrightarrow{Oy}|$. Also, the functions O_n^m and $\widetilde{I}_n^m$, together with a related function I_n^m, are defined as follows:

$$O_n^m(\overrightarrow{Ox}) = h_n^{(1)}(k|\overrightarrow{Ox}|)Y_n^m\left(\frac{\overrightarrow{Ox}}{|\overrightarrow{Ox}|}\right),$$

$$\widetilde{I}_n^m(\overrightarrow{Ox}) = j_n(k|\overrightarrow{Ox}|)\overline{Y}_n^m\left(\frac{\overrightarrow{Ox}}{|\overrightarrow{Ox}|}\right), \quad I_n^m(\overrightarrow{Ox}) = j_n(k|\overrightarrow{Ox}|)Y_n^m\left(\frac{\overrightarrow{Ox}}{|\overrightarrow{Ox}|}\right), \tag{11}$$

where $h_n^{(1)}$ and j_n stand for the spherical Hankel function of the first kind and nth order and the spherical Bessel function of the nth order, respectively. Also, Y_n^m denotes the spherical harmonics.

The functions O_n^m and $\widetilde{I}_n^m$ allow the following expansions:

$$\widetilde{I}_n^m(\overrightarrow{O'y}) = \sum_{n'=0}^{\infty} \sum_{m'=-n'}^{n'} \sum_{l \in \mathcal{W}(n,n',m,m')} (2n'+1)(-1)^{m'} W_{n,n',m,m',l}\widetilde{I}_{n'}^{-m'}(\overrightarrow{Oy})I_l^{-m-m'}(\overrightarrow{O'O}), \tag{12}$$

$$O_n^m(\overrightarrow{Ox}) = \sum_{n'=0}^{\infty} \sum_{m'=-n'}^{n'} \sum_{l \in \mathcal{W}(n,n',m,m')} (2n'+1)(-1)^{m+n'} W_{n,n',m,m',l}I_{n'}^{-m'}(\overrightarrow{xx_0})O_l^{m+m'}(\overrightarrow{Ox_0}). \tag{13}$$

In (13), we have assumed $|\overrightarrow{xx_0}| < |\overrightarrow{Ox_0}|$. In these formulae, $W_{n,n',m,m',l}$ is a number related to the Wigner 3-j symbol [15] (the number given by $\begin{pmatrix} \cdots \\ \cdots \end{pmatrix}$ in the following) as follows:

$$W_{n,n',m,m',l} = (2l+1)i^{n'-n+l} \begin{pmatrix} n & n' & l \\ 0 & 0 & 0 \end{pmatrix} \begin{pmatrix} n & n' & l \\ m & m' & -m-m' \end{pmatrix}.$$

Also, the set $\mathcal{W}(n,n',m,m')$ in (12) and (13) is defined by

$$\mathcal{W}(n,n',m,m') = \{l|l \in \mathbb{Z}, \ n+n'+l : \text{even}, \ \max\{|m+m'|,|n-n'|\} \leqslant l \leqslant n+n'\}.$$

We next derive multipole expansions for $\boldsymbol{E}$ and $\boldsymbol{H}$. To this end it is convenient to start from alternative integral representations for $\boldsymbol{E}$ and $\boldsymbol{H}$ given below:

$$E_i(x) = -\frac{1}{k^2}e_{ikj}\frac{\partial}{\partial x_k}\int_{\partial D_i}\left(-e_{pqr}e_{rsj}\frac{\partial}{\partial y_s}\frac{\partial}{\partial y_q}G(x-y)m_p(y) + i\omega\mu^i e_{pqj}\frac{\partial}{\partial y_q}G(x-y)j_p(y)\right)dS_y, \tag{14}$$

$$H_i(x) = -\frac{e_{iuv}e_{vkj}}{i\omega\mu^i k^2}\frac{\partial}{\partial x_u}\frac{\partial}{\partial x_k}\int_{\partial D_i}\left(-e_{pqr}e_{rsj}\frac{\partial}{\partial y_s}\frac{\partial}{\partial y_q}G(x-y)m_p(y) + i\omega\mu^i e_{pqj}\frac{\partial}{\partial y_q}G(x-y)j_p(y)\right)dS_y. \tag{15}$$

Substitution of (10) in (14) and (15) shows that the following definition for the multipole moments around O, denoted by $M_{i,n,m}(O)$, is suitable:

$$M_{j,n,m}(O) = \int\left(-e_{pqr}e_{rsj}\frac{\partial}{\partial y_q}\frac{\partial}{\partial y_s}\widetilde{I}_n^m(\overrightarrow{Oy})m_p(y) + i\omega\mu^i e_{pqj}\frac{\partial}{\partial y_q}\widetilde{I}_n^m(\overrightarrow{Oy})j_p(y)\right)dS_y. \tag{16}$$

These multipole moments are transformed into the coefficients of the local expansion via the following formula (M2L)

$$L_{j,n,m}(x_0) = \sum_{n'=0}^{\infty}\sum_{m'=-n'}^{n'}\sum_{l\in\mathcal{W}(n',n,m',m)}(2n'+1)W_{n',n,m',m,l}\widetilde{O}_l^{-m-m'}(\overrightarrow{Ox_0})M_{j,n',m'}(O), \tag{17}$$

which is derived with the help of (13). With these coefficients one computes E and H using the following local expansions:

$$E_i(x) = -\frac{i}{4\pi k}\sum_n\sum_m(2n+1)L_{j,n,m}(O')e_{ikj}\frac{\partial}{\partial x_k}\widetilde{I}_m^n(\overrightarrow{O'x}), \tag{18}$$

$$H_i(x) = -\frac{1}{4\pi\omega\mu k}\sum_n\sum_m(2n+1)L_{j,n,m}(O')e_{iuv}e_{vkj}\frac{\partial}{\partial x_u}\frac{\partial}{\partial x_k}\widetilde{I}_m^n(\overrightarrow{O'x}). \tag{19}$$

The FMM algorithm requires us to shift the origin of multipole and local expansions. The formula for shifting the origin of the multipole moments (M2M) is obtained from (12) in the following form:

$$M_{j,n,m}(O') = \sum_{n'=0}^{\infty}\sum_{m'=-n'}^{n'}\sum_{l\in\mathcal{W}(n,n',m,m')}(2n'+1)(-1)^{m'}W_{n,n',m,m',l}I_l^{-m-m'}(\overrightarrow{O'O})M_{j,n',-m'}(O). \tag{20}$$

Similarly, we derive the shift formula for the coefficients of the local expansion (L2L) in the following form:

$$L_{j,n,m}(x_1) = \sum_{n'=0}^{\infty}\sum_{m'=-n'}^{n'}\sum_{l\in\mathcal{W}(n',n,m',-m)}(-1)^m(2n'+1)W_{n',n,m',-m,l}I_l^{m-m'}(\overrightarrow{x_0x_1})L_{j,n',m'}(x_0). \tag{21}$$

Use of the above formulae as they are, truncating the infinite series with p terms, would result in an algorithm with $O(p^5)$ complexity. In our implementation, however, we reduce this complexity to $O(p^3)$ by using rotations of the coordinates and recursive formulae as discussed in Gumerov and Duraiswami [16].

We next present the diagonal form. To this end we prepare the plane wave expansion of the fundamental solution G of Helmholtz' equation in 3D given as follows:

$$G(x-y) = \frac{ik}{(4\pi)^2}\int_{|\hat{k}|=1}e^{i(x-X)\cdot k}\left(\sum_n\sum_m i^n(2n+1)\overline{Y_n^m}(\hat{k})O_n^m(X-Y)\right)e^{-i(y-Y)\cdot k}dS_{\hat{k}}, \tag{22}$$

where $k = k\hat{k}$ and X and Y are points near x and y, respectively. The expression within the large parentheses on the RHS of the above formula can be rewritten in the following form:

$$\sum_{n\geq 0}i^n(2n+1)P_n\left(\hat{k}\cdot\frac{X-Y}{|X-Y|}\right)h_n^{(1)}(k|X-Y|), \tag{23}$$

where P_n is the Legendre polynomial of the order n. Also, we have the following expansion of the plane wave in terms of the functions introduced in (11):

$$e^{ix\cdot k} = \sum_{n=0}^{\infty}\sum_{m=-n}^{n}i^n(2n+1)\widetilde{I}_n^m(x)Y_n^m(\hat{k}). \tag{24}$$

We now proceed to the formulation of the diagonal form. The formulae for the plane wave expansion in (22) and a series expansion of $e^{ix \cdot k}$ in (24) are substituted in the integral representations for E and H in (14) and (15) to yield the diagonal form version of the multipole moments, denoted by $\widetilde{F}_j(\theta, \phi, O)$, in the following form (M2F):

$$\widetilde{F}_j(\theta, \phi, O) = \sum_{n=0}^{\infty} \sum_{m=-n}^{n} i^{-n}(2n+1)Y_n^m(\theta, \phi)M_{j,n,m}(O), \tag{25}$$

where θ and ϕ are the polar coordinates for the unit vector $\hat{k}$ (i.e. $\hat{k} = (1, \theta, \phi)$). One then uses (22) and (23) to convert $\widetilde{F}_j(\theta, \phi, O)$ into the diagonal form version of the coefficients of the local expansion denoted by $\widetilde{H}_j(\theta, \phi, x_0)$ in the following manner (F2H):

$$\widetilde{H}_j(\theta, \phi, x_0) = \widetilde{F}_j(\theta, \phi, O) \sum_{n \geq 0} i^n(2n+1)P_n\left(\hat{k} \cdot \frac{\overrightarrow{Ox_0}}{|\overrightarrow{Ox_0}|}\right)h_n^{(1)}(k|\overrightarrow{Ox_0}|). \tag{26}$$

Finally, the conversion from the coefficients of the local expansion for the diagonal form into those of the low frequency FMM is done with the following formula (H2L):

$$L_{j,n,m}(x_0) = \frac{i^n}{4\pi} \int_{|\hat{k}|=1} \widetilde{H}_j(\theta, \phi, x_0)Y_n^m(\hat{k}) \, dS_{\hat{k}}. \tag{27}$$

In addition to these formulae, we use (22) to obtain the formula for the shift of the origin for $\widetilde{F}_j$ (F2F) in the following form:

$$\widetilde{F}_j(\theta, \phi, y_1) = \widetilde{F}_j(\theta, \phi, y_0)e^{-ik\hat{k} \cdot \overrightarrow{y_1 y_0}}. \tag{28}$$

Similarly, the shift of the origin formula for $\widetilde{H}_j$ is given by the following expression (H2H):

$$\widetilde{H}_j(\theta, \phi, x_1) = \widetilde{H}_j(\theta, \phi, x_0)e^{ik\hat{k} \cdot \overrightarrow{x_0 x_1}}. \tag{29}$$

2.2. Formulation of the periodic boundary value problems

We next consider the FMM formulation for periodic boundary value problems. We assume, for the purpose of simplicity, that the domain under consideration is periodic in two mutually perpendicular directions and that the periods in these two directions are equal. We denote this period by L. Also, we take a cartesian coordinate system in a way that the directions of the periodicity coincide with the x_2 and x_3 coordinate directions. It might appear more natural to take the x_3 axis perpendicular to the plane of the periodicity in view of the expressions for the lattice sums which use the spherical harmonics; these functions are 'isotropic' only in $x_{1,2}$ directions. A careful comparison shows, however, that there is little difference in the efficiency of the algorithms resulting from these choices of the coordinate systems. We therefore decided to choose the axis in this manner considering the ease of computing S_{ml}^3 resulting from the δ_{m0} factor as we shall see in the Appendix (see (41)).

2.2.1. Statement of the problem

Let D be the domain defined by

$$D = (-\infty, \infty) \otimes (-L/2, L/2) \otimes (-L/2, L/2)$$

which is further subdivided into N subdomains $D = \overline{D_1 \cup D_2 \cup \cdots \cup D_N}$ (Fig. 2). The fields within these subdomains satisfy Maxwell's equations given by (1) and (2). The subdomain which extends to $x_1 \to -\infty$ is denoted by D_I where we consider the incident plane wave of the following forms:

$$E^{\text{inc}} = a^{\text{inc}}e^{ik^{\text{inc}} \cdot x}, \qquad H^{\text{inc}} = b^{\text{inc}}e^{ik^{\text{inc}} \cdot x}.$$

On the periodic boundaries given by $S_p = \{x| \ x \in \partial D, \ |x_2| = L/2 \text{ or } |x_3| = L/2\}$ we require the following periodic boundary conditions:

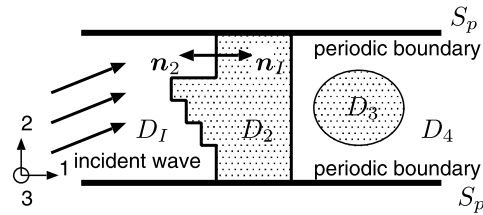Fig. 2. Periodic boundary value problems.

$$E(x_1, L/2, x_3) = e^{i\beta_2} E(x_1, -L/2, x_3),$$
$$E(x_1, x_2, L/2) = e^{i\beta_3} E(x_1, x_2, -L/2),$$
$$H(x_1, L/2, x_3) = e^{i\beta_2} H(x_1, -L/2, x_3),$$
$$H(x_1, x_2, L/2) = e^{i\beta_3} H(x_1, x_2, -L/2),$$

where β_i is the phase difference of the incident wave at $x_i = -L/2$ and $x_i = L/2$, expressed by

$$\beta_i = Lk_i^{\mathrm{inc}}, \quad i = 2, 3.$$

2.2.2. Periodic Green's function

The two periodic Green's function for Maxwell's equations is denoted by Γ_{ip}^{P}. The function Γ_{ip}^{P} satisfies the governing equation and the periodic boundary conditions given by

$$e_{ijk} e_{klm} \Gamma_{mp,lj}^{\mathrm{P}}(x - y) - k^2 \Gamma_{ip}^{\mathrm{P}}(x - y) = \delta_{ip}\delta(x - y),$$

$$\Gamma_{ip}^{\mathrm{P}}(x_1, L/2, x_3) = e^{i\beta_2} \Gamma_{ip}^{\mathrm{P}}(x_1, -L/2, x_3), \tag{30}$$

$$\Gamma_{ip}^{\mathrm{P}}(x_1, x_2, L/2) = e^{i\beta_3} \Gamma_{ip}^{\mathrm{P}}(x_1, x_2, -L/2), \tag{31}$$

$$\frac{\partial \Gamma_{ip}^{\mathrm{P}}}{\partial x_2}(x_1, L/2, x_3) = e^{i\beta_2} \frac{\partial \Gamma_{ip}^{\mathrm{P}}}{\partial x_2}(x_1, -L/2, x_3), \tag{32}$$

$$\frac{\partial \Gamma_{ip}^{\mathrm{P}}}{\partial x_3}(x_1, x_2, L/2) = e^{i\beta_3} \frac{\partial \Gamma_{ip}^{\mathrm{P}}}{\partial x_3}(x_1, x_2, -L/2). \tag{33}$$

The function Γ_{ip}^{P} is easily seen to be expressed in terms of the following lattice sums:

$$\Gamma_{ip}^{\mathrm{P}}(x - y) = \sum_{\omega \in \mathcal{L}} \Gamma_{ip}(x - y - \omega) e^{i\beta \cdot \omega}, \tag{34}$$

where $\mathcal{L}$ stands for the lattice points defined by $\mathcal{L} = \{(0, \omega_2, \omega_3) | \ \omega_2 = pL, \ \omega_3 = qL, \ p, q \in \mathbb{Z}\}$. Γ_{ip}^{P} can also be written in the following form:

$$\Gamma_{ip}^{\mathrm{P}}(x - y) = \left(\frac{1}{k^2} \frac{\partial}{\partial x_i} \frac{\partial}{\partial x_p} + \delta_{ip} \right) G^{\mathrm{P}}(x - y),$$

where G^{P} is the periodic Green function for Helmholtz' equation in 3D which allows the following expression in terms of a lattice sum:

$$G^{\mathrm{P}}(x - y) = \sum_{\omega \in \mathcal{L}} \frac{e^{ik|x - y - \omega|}}{4\pi|x - y - \omega|} e^{i\beta \cdot \omega}.$$

2.2.3. Boundary integral equation

The continuity of the tangential components of E and H on interfaces between subdomains gives the following variational integral equations:

$$0 = \sum_d \left(\delta_{dI} \int_{\partial D_d \setminus S_p} \boldsymbol{t}^d(x) \cdot \boldsymbol{E}^{\mathrm{inc}}(x) \, \mathrm{d}S_x + \int_{\partial D_d \setminus S_p} \int_{\partial D_d \setminus S_p} \left\{ \boldsymbol{t}^d(x) \cdot (\boldsymbol{m}^d(y) \times \nabla_y G_d^{\mathrm{P}}(\boldsymbol{x} - \boldsymbol{y})) \right. \right.$$

$$\left. \left. -\mathrm{i}\omega\mu^d \boldsymbol{t}^d(x) \cdot \boldsymbol{j}^d(y) G_d^{\mathrm{P}}(\boldsymbol{x} - \boldsymbol{y}) + \frac{\mathrm{i}}{\omega\epsilon^d} \operatorname{div}_S \boldsymbol{t}^d(x) \operatorname{div}_S \boldsymbol{j}^d(y) G_d^{\mathrm{P}}(\boldsymbol{x} - \boldsymbol{y}) \right\} \mathrm{d}S_y \, \mathrm{d}S_x \right), \tag{35}$$

$$0 = \sum_d \left(\delta_{dI} \int_{\partial D_d \setminus S_p} \boldsymbol{t}^d(x) \cdot \boldsymbol{H}^{\mathrm{inc}}(x) \, \mathrm{d}S_x + \int_{\partial D_d \setminus S_p} \int_{\partial D_d \setminus S_p} \left\{ -\boldsymbol{t}^d(x) \cdot (\boldsymbol{j}^d(y) \times \nabla_y G_d^{\mathrm{P}}(\boldsymbol{x} - \boldsymbol{y})) \right. \right.$$

$$\left. \left. -\mathrm{i}\omega\epsilon^d \boldsymbol{t}^d(x) \cdot \boldsymbol{m}^d(y) G_d^{\mathrm{P}}(\boldsymbol{x} - \boldsymbol{y}) + \frac{\mathrm{i}}{\omega\mu^d} \operatorname{div}_S \boldsymbol{t}^d(x) \operatorname{div}_S \boldsymbol{m}^d(y) G_d^{\mathrm{P}}(\boldsymbol{x} - \boldsymbol{y}) \right\} \mathrm{d}S_y \, \mathrm{d}S_x \right) \tag{36}$$

where $\boldsymbol{t}^d$ is defined as in (9). In addition, we require $\mathrm{e}^{-\mathrm{i}\boldsymbol{\beta}}$-periodicity to $\boldsymbol{T}'$ when $\boldsymbol{T}'$ extends beyond S_p. Note that these integral equations include no unknowns on S_p.

2.2.4. Periodic FMM

We now consider a particular subdomain D_a and assume, for the purpose of simplicity, that the boundary $\partial D_a \setminus S_p$ is included in a cube whose edges are of lengths L and are parallel to the coordinate axes. The cube thus introduced is called the unit cell. The assumption that $\partial D_a \setminus S_p$ is included in one cubic unit cell, however, is not essential and can be removed without much difficulty.

From the lattice sum expression for Γ_{ip}^{P} in (34) we see that the periodic boundary value problems can be interpreted as an ordinary problem in an infinite domain with an infinite repetition of the replicas of the unit cell (Fig. 3).

We now take the unit cell as the level 0 cell in FMM, and divide the set of replica cells into those adjacent to the unit cell (denoted by C_N) and others (denoted by C_F). Correspondingly, the sum in Γ^{P} is divided into the contribution from C_N, denoted by Γ^{PN} which includes the contributions from the unit cell itself, and those from C_F, denoted by Γ^{PF}. Namely, we have

$$\Gamma_{ij}^{\mathrm{P}} = \Gamma_{ij}^{\mathrm{PF}} + \Gamma_{ij}^{\mathrm{PN}},$$

where

$$\Gamma_{ij}^{\mathrm{PF}}(\boldsymbol{x} - \boldsymbol{y}) = \sum_{\boldsymbol{\omega} \in \mathcal{L}'} \Gamma_{ij}(\boldsymbol{x} - \boldsymbol{y} - \boldsymbol{\omega}) \mathrm{e}^{\mathrm{i}\boldsymbol{\beta} \cdot \boldsymbol{\omega}},$$

$$\Gamma_{ij}^{\mathrm{PN}}(\boldsymbol{x} - \boldsymbol{y}) = \sum_{\boldsymbol{\omega} \in \mathcal{L}''} \Gamma_{ij}(\boldsymbol{x} - \boldsymbol{y} - \boldsymbol{\omega}) \mathrm{e}^{\mathrm{i}\boldsymbol{\beta} \cdot \boldsymbol{\omega}},$$

$\mathcal{L}' = \{(0, \omega_2, \omega_3) | \omega_2 = pL, \ \omega_3 = qL, \ p, q \in \mathbb{Z}, \ |p| \geqslant 2 \text{ or } |q| \geqslant 2\}$ and $\mathcal{L}'' = \mathcal{L} \setminus \mathcal{L}'$.

The evaluation of $\Gamma_{ij}^{\mathrm{PN}}(\boldsymbol{x} - \boldsymbol{y})$ can be carried out using the standard FMM, and needs no further consideration. Hence, we focus on the computation of $\Gamma_{ij}^{\mathrm{PF}}(\boldsymbol{x} - \boldsymbol{y})$ in the rest of this section.

We first consider the diagonal forms. We start from the plane wave expansion for the fundamental solution Γ_{ip} given below:
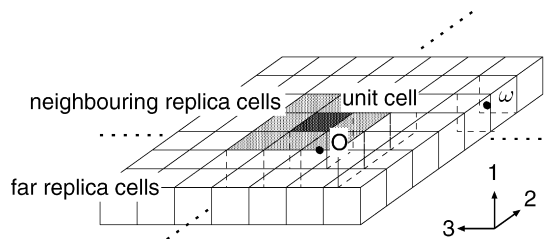

Fig. 3. Replica cells.

$$\Gamma_{ij}(\boldsymbol{x} - \boldsymbol{y}) = -\frac{1}{k^2} e_{jpk} e_{kqi} \frac{\partial}{\partial x_p} \frac{\partial}{\partial y_q} G(\boldsymbol{x} - \boldsymbol{y})$$

$$= -\frac{\mathrm{i}k}{(4\pi)^2} \int_{|\hat{\boldsymbol{k}}|=1} \left(e_{jpk} \frac{\partial}{\partial x_p} \mathrm{e}^{\mathrm{i}(\boldsymbol{x} - \boldsymbol{X}) \cdot \boldsymbol{k}} \right)$$

$$\times \underbrace{\left(\sum_n \sum_m \mathrm{i}^n (2n+1) \overline{Y_n^m}(\hat{\boldsymbol{k}}) O_n^m(\boldsymbol{X} - \boldsymbol{Y}) \right)}_{\text{F2H formula}} \left(e_{kqi} \frac{\partial}{\partial y_q} \mathrm{e}^{-\mathrm{i}(\boldsymbol{y} - \boldsymbol{Y}) \cdot \boldsymbol{k}} \right) \mathrm{d}S_{\hat{\boldsymbol{k}}}.$$

The factor within the second parentheses on the RHS corresponds to the F2H formula. As one substitutes the above formula into (34) one obtains the plane wave expansion of $\Gamma_{ij}^{\mathrm{PF}}$ in the following form:

$$\Gamma_{ij}^{\mathrm{PF}}(\boldsymbol{x} - \boldsymbol{y}) = -\frac{\mathrm{i}k}{(4\pi)^2} \int_{|\hat{\boldsymbol{k}}|=1} \left(e_{jpk} \frac{\partial}{\partial x_p} \mathrm{e}^{\mathrm{i}\boldsymbol{x} \cdot \boldsymbol{k}} \right)$$

$$\times \underbrace{\left(\sum_n \sum_m \mathrm{i}^n (2n+1) \overline{Y_n^m}(\hat{\boldsymbol{k}}) \left(\sum_{\boldsymbol{\omega} \in \mathcal{L}'} O_n^m(-\boldsymbol{\omega}) \mathrm{e}^{\mathrm{i}\boldsymbol{\beta} \cdot \boldsymbol{\omega}} \right) \right)}_{\text{Periodised F2H formula}} \left(e_{kqi} \frac{\partial}{\partial y_q} \mathrm{e}^{-\mathrm{i}\boldsymbol{y} \cdot \boldsymbol{k}} \right) \mathrm{d}S_{\hat{\boldsymbol{k}}}.$$

From this equation we see that the contribution from the non-adjacent replica cells is evaluated with the periodised F2H formula given below:

$$\widetilde{H}_j(\theta, \phi, O) = \widetilde{F}_j(\theta, \phi, O) \sum_{n \geq 0} \sum_{m=-n}^{n} \mathrm{i}^n (2n+1) \overline{Y_n^m}(\hat{\boldsymbol{k}}) \left(\sum_{\boldsymbol{\omega} \in \mathcal{L}'} O_n^m(-\boldsymbol{\omega}) \mathrm{e}^{\mathrm{i}\boldsymbol{\beta} \cdot \boldsymbol{\omega}} \right), \tag{37}$$

where $\widetilde{F}_j(\theta, \phi, O)$ is the multipole moment of the level 0 cell (namely, the unit cell) and $\widetilde{H}_j(\theta, \phi, O)$ is the coefficient of the local expansion of the level 0 cell.

Similarly, one obtains the periodised M2L formula in the low frequency FMM in the following form:

$$L_{j,n,m}(O) = \sum_{n'=0}^{\infty} \sum_{m'=-n'}^{n'} \sum_{l \in \mathcal{W}(n',n,m',m)} (2n'+1) W_{n',n,m',m,l} \left(\sum_{\boldsymbol{\omega} \in \mathcal{L}'} \widetilde{O}_l^{-m-m'}(-\boldsymbol{\omega}) \mathrm{e}^{\mathrm{i}\boldsymbol{\beta} \cdot \boldsymbol{\omega}} \right) M_{j,n',m'}(O), \tag{38}$$

where $M_{j,n,m}(O)$ is the multipole moment of the level 0 cell and $L_{j,n,m}(O)$ is the coefficient of the local expansion of the level 0 cell.

Eqs. (37) and (38) show that the formulation of the periodic FMM is completed once one finds a way to evaluate the lattice sum

$$\sum_{\boldsymbol{\omega} \in \mathcal{L}'} \widetilde{O}_n^m(-\boldsymbol{\omega}) \mathrm{e}^{\mathrm{i}\boldsymbol{\beta} \cdot \boldsymbol{\omega}} \tag{39}$$

efficiently. It is quite impractical to compute this lattice sum as is, since the convergence of this series is extremely slow. We here propose to evaluate this lattice sum with the help of Fourier analysis, the details of which are presented in the Appendix. For other approaches to compute lattice sums of the form in (39) the reader is referred to Enoch et al. [17], for example.

3. Algorithm

In this paper we shall use both diagonal forms and the low frequency FMM switching between these formulations depending on the size of cells as proposed by Otani and Nishimura [12]. Namely, we use diagonal forms in the level l if $kd^l \geq C_{\mathrm{dia}}$ is satisfied, where d^l is the edge length of the cell at the level l. In levels where $kd^l < C_{\mathrm{dia}}$ holds, on the other hand, we use the low frequency FMM. In this approach the number C_{dia} is a parameter which determines the level where we switch between formulations. In the present investigation we use $C_{\mathrm{dia}} = 28$. This number has been determined numerically so that the relative error defined as

$$\frac{|S(\boldsymbol{x} - \boldsymbol{y}) - G(\boldsymbol{x} - \boldsymbol{y})|}{|G(\boldsymbol{x} - \boldsymbol{y})|}$$

does not exceed 10^{-5} for $^\forall x \in C_1^l$, $^\forall y \in C_2^l$ for any combination of (C_1^l, C_2^l), where C_1^l is a cell in the level l and C_2^l is another in the interaction list of C_1^l. In the above expression, S is the approximant of G calculated with the diagonal form in which the infinite series in (23) is truncated with $2p$ terms. The algorithm for this approach is indicated schematically in Fig. 4 which explains the case with $kd^0 > C_{\text{dia}}$ and in Fig. 5 which considers the $kd^0 \leqslant C_{\text{dia}}$ case.

The algorithm for the periodic FMM goes as follows: In the upward pass we consider only those cells in the unit cell, and use the same algorithm as in the ordinary FMM except that we go up to the level 0 cell.

In the downward pass for the periodic FMM, we have to take into consideration not just the effects from the cells in the unit cell, but also those from all other replica cells, whose multipole moments are the same as those of the original cell in the unit cell except for the $e^{i\beta \cdot \omega}$ factor. As in the previous section, we divide the replica cells into those adjacent to the unit cell (C_N) and others (C_F). The contribution from C_F is evaluated at the level 0 with the help of the periodised M2L or F2H formulae. The contribution from C_N is evaluated in the downward pass. For this purpose we extend the definition of the interaction list so that it contains nearby cells in the replicas included in C_N. Fig. 6 shows the interaction list for the ordinary FMM and the extended interaction list for the periodic FMM. The above algorithm is explained in the following Fortran-like pseudocode.

```
! upward pass
  do level = bottom_level, 0, −1
    do icell = all the cells in the current level
    if (icell is a leaf) then
       Use (16) and (25) to compute the multipole moments
    else
       Use (20) or (28) to add the multipole moments of the children to the multipole
       moments of icell (M2M, F2F)
    endif
    enddo
    if (level=switching level) then
       Use (25) to convert the multipole moments for low frequency FMM to the multipole
       moments for the diagonal form (M2F)
    endif
  enddo
  ! level = 0
  Use (37) or (38) to convert the multipole moments of the replica cells to the coeffi-
  cient of the local expansion (periodised F2H, M2L)
  ! downward pass
  do level = 1, bottom_level
    do icell = all the cells in the current level
```
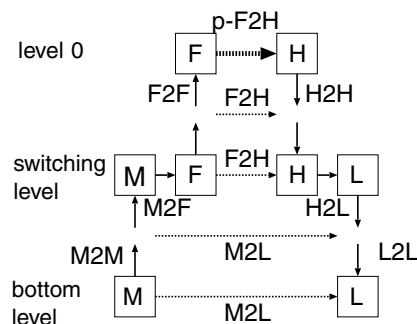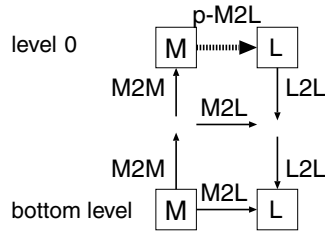

Fig. 4. Algorithm (with diagonal form).

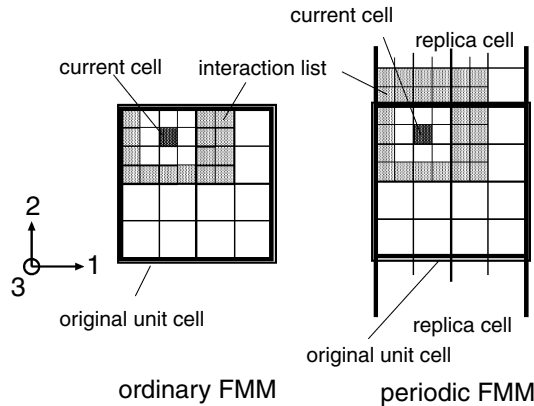Fig. 5. Algorithm (with low frequency FMM).

Fig. 6. Interaction list.

- Use (21) or (29) to convert the coefficients of the local expansion of the parent cell to those of icell (L2L, H2H)
- Use (17) or (26) to convert the multipole moments of the cells within the extended interaction list to the coefficients of the local expansion of icell (M2L, F2H)

    if (icell is a leaf) **then**
      Use (18), (19) and (27) to evaluate the potentials
    endif
  enddo
  if (level = switching level) **then**
    Use (27) to convert the coefficients of the local expansion for the diagonal form to those of the low frequency FMM (H2L)
  endif
enddo

4. Far fields

In the limit of $x_1 \to \pm\infty$, the fields $\boldsymbol{E}$ and $\boldsymbol{H}$ allow the following expressions in terms of the superposition of plane waves:

$$\boldsymbol{E}^{\pm} = \sum_n \hat{\boldsymbol{a}}_n^{\pm} e^{i\boldsymbol{k}_n^{\pm}\cdot\boldsymbol{x}} + \delta_{\pm}\boldsymbol{E}^{\mathrm{inc}}, \qquad \boldsymbol{H}^{\pm} = \sum_n \hat{\boldsymbol{b}}_n^{\pm} e^{i\boldsymbol{k}_n^{\pm}\cdot\boldsymbol{x}} + \delta_{\pm}\boldsymbol{H}^{\mathrm{inc}}, \tag{40}$$

where n is a multiple index defined by $n = (n_2, n_3)$, $\delta_+ = 0$, $\delta_- = 1$ and $\hat{\boldsymbol{a}}_n^{\pm}$ and $\hat{\boldsymbol{b}}_n^{\pm}$ are vectors such that the relation

$$\hat{\boldsymbol{b}}_n^{\pm} = \frac{1}{\omega\mu^{\pm}} \boldsymbol{k}_n^{\pm} \times \hat{\boldsymbol{a}}_n^{\pm}$$

holds. Also, $\boldsymbol{k}_n^\pm$ is given by

$$\boldsymbol{k}_n^\pm = \begin{pmatrix} \pm\sqrt{k_\pm^2 - \frac{1}{L^2}(\beta_2 + 2n_2\pi)^2 - \frac{1}{L^2}(\beta_3 + 2n_3\pi)^2} \\ \frac{1}{L}(\beta_2 + 2n_2\pi) \\ \frac{1}{L}(\beta_3 + 2n_3\pi) \end{pmatrix},$$

where $k_\pm$ stands for the wave number for $D_\pm$ and $D_\pm$ indicates the subdomain of D containing $x_1 = \pm\infty$. The summation in (40) is taken over such $n = (n_2, n_3)$ that the vector $\boldsymbol{k}_n^\pm$ is real. Fig. 7 shows a schematic view of the far fields.

We now consider an inspection surface indicated by dashed lines in Fig. 7 and call the part of $D_\pm$ within the inspection surface as $D_\pm'$. We then have the following Green's formula:

$$\int_{\partial D_\pm'} \left((\nabla \times \boldsymbol{E}_\pm^1) \cdot (\boldsymbol{E}_\pm^2 \times \boldsymbol{n}) - (\nabla \times \boldsymbol{E}_\pm^2) \cdot (\boldsymbol{E}_\pm^1 \times \boldsymbol{n}) \right) \mathrm{d}S = 0.$$

We now substitute the far field expression in (40) into $\boldsymbol{E}^1$ and the following function into $\boldsymbol{E}^2$ in the above Green's formula:

$$\boldsymbol{E}_\pm^2 = \tilde{\boldsymbol{a}}_m \mathrm{e}^{-\mathrm{i}\boldsymbol{k}_m^\pm \cdot \boldsymbol{x}}.$$

As we take the limit of letting the left and right ends of D_-' and D_+', respectively, tend to infinity in the resulting equation (See Fig. 7. The surfaces thus introduced at the points of infinity are denoted by $S_{\pm\infty}$), we obtain the following formula:

$$\tilde{\boldsymbol{a}}_m^\pm \cdot \hat{\boldsymbol{a}}_m^\pm = \frac{\omega\mu^\pm}{2L^2(\boldsymbol{k}_m^\pm)_1} \int_{\partial D_\pm' \backslash (S_p \cup S_{\pm\infty})} \boldsymbol{n} \cdot \left(\boldsymbol{m}_2^\pm \times \boldsymbol{j}_1 - \boldsymbol{m}_1 \times \boldsymbol{j}_2^\pm \right) \mathrm{d}S,$$

where $\boldsymbol{j}_1$ and $\boldsymbol{m}_1$ are the surface electric and magnetic currents obtained as the numerical solution to the boundary integral equations and $\boldsymbol{j}_2^\pm$ and $\boldsymbol{m}_2^\pm$ are given as

$$\boldsymbol{j}_2^\pm = -\frac{1}{\omega\mu^\pm} \boldsymbol{n} \times (\boldsymbol{k}_m^\pm \times \tilde{\boldsymbol{a}}_m^\pm) \mathrm{e}^{-\mathrm{i}\boldsymbol{k}_m^\pm \cdot \boldsymbol{x}}, \qquad \boldsymbol{m}_2^\pm = (\tilde{\boldsymbol{a}}_m^\pm \times \boldsymbol{n}) \mathrm{e}^{-\mathrm{i}\boldsymbol{k}_m^\pm \cdot \boldsymbol{x}}.$$

By taking two unit vectors orthogonal to $\boldsymbol{k}_m^\pm$ as $\tilde{\boldsymbol{a}}_m^\pm$, consecutively, and by computing $\tilde{\boldsymbol{a}}_m^\pm \cdot \hat{\boldsymbol{a}}_m^\pm$ for these cases, we obtain $\hat{\boldsymbol{a}}_m^\pm$.

The amount of energy which passes through the plane $S_{\pm\infty}$ at infinity is computed with the following formula:

$$\mathrm{Re} \int_{S_{\pm\infty}} (\boldsymbol{E}^\pm \times \overline{\boldsymbol{H}}^\pm) \cdot \boldsymbol{n}^{\pm\infty} \mathrm{d}S = L^2 \sum_n \mathrm{Re}(\hat{\boldsymbol{a}}_n^\pm \times \overline{\hat{\boldsymbol{b}}}_n^\pm) \cdot \boldsymbol{n}^{\pm\infty}.$$
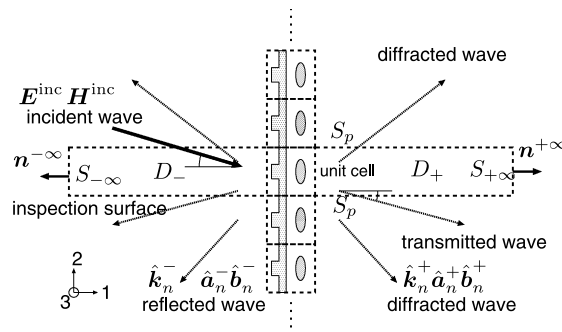

Fig. 7. Far fields.

5. Numerical examples

In this section we shall present numerical examples obtained with the present formulation. We first state techniques common to all the examples.

- As an iterative solver for linear equations we use Flexible GMRES (FGMRES) [18]. FGMRES differs from the standard GMRES in that one can use different preconditioners for each of the iteration steps. This means that one can precondition using iterative solvers. The criterion of convergence for FGMRES is set to be 10^{-3} times the initial value unless stated otherwise. As the preconditioner we use the part of the matrix computed directly in the FMM algorithm. The inversion in the process of preconditioning is carried out approximately using GMRES, which we terminate after 100 iterations or when the norm of the error is less than 10^{-1} times its initial value except in the cases of woodpile crystals. See Section 5.2.3 for the parameters used in the woodpile case.
- In this paper we expand **m** and **j** in the integral equations in (35) and (36) using the Rao–Wilton–Glisson basis function [19], which is a standard choice in the boundary integral approaches for Maxwell's equations. Also, we have used Galerkin's method to discretise the integral equations in (35) and (36). Namely, we have used the Rao–Wilton–Glisson basis functions to $t(x^0)$, as well.
- For the calculation we use FUJITSU PRIMEPOWER HPC2500 supercomputer of Academic Center for Computing and Media Studies of Kyoto University. The code is OpenMP parallelised and the number of CPUs used is 8 for sphere problems and 32 for others.

5.1. Verification

We first verify our approach by solving problems with known analytical solutions. The model we consider is the dielectric layers of parallel slabs shown in Fig. 8. The unit of the periodicity is as shown in Fig. 9, in which the (relative) dielectric constants and wave numbers are also given.

For the mesh we use 83,408 planar triangular elements whose edge length is approximately 1/12 of the wavelength. The total degrees of freedom are 250,224. As the criterion of convergence for FGMRES we test both 10^{-3} and 10^{-4}.

The numerical results are shown in Table 1. The 'error' in this table indicates the average of the errors, relative to the exact solution, of the surface electric and magnetic current vectors **j** and **m** computed at the centroid of the elements. The error is small for either of the convergence criteria of FGMRES (10^{-3} or 10^{-4}). From this result we conclude that the present approach is sufficiently accurate for engineering purposes.

Fig. 10 indicates the mode of convergence for FGMRES. This figure shows that the convergence starts to slow down when the residual is below 0.6×10^{-3} times the initial value. It is considered to be an important future work to find more effective preconditioners and criteria for the termination in FGMRES.
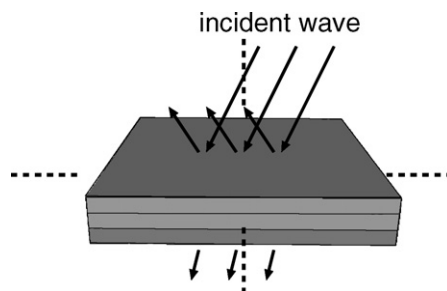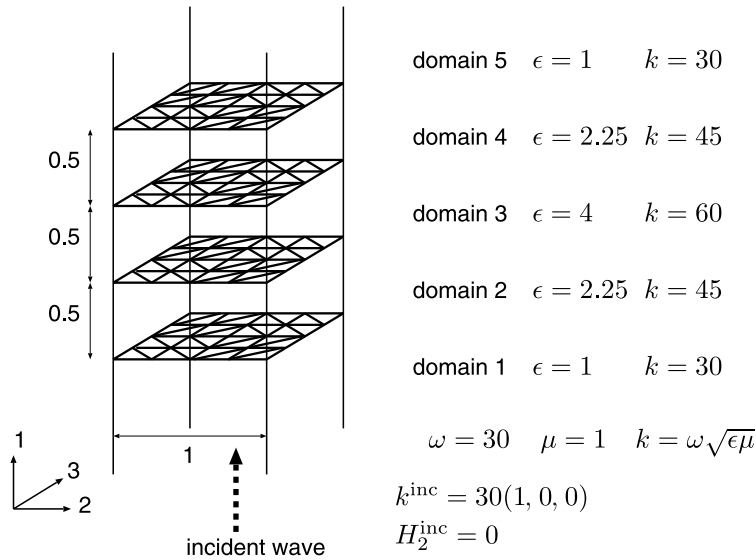

Fig. 8. Dielectric layers of slabs.

Fig. 9. Model of dielectric layers of slabs.

Table 1
Numerical results

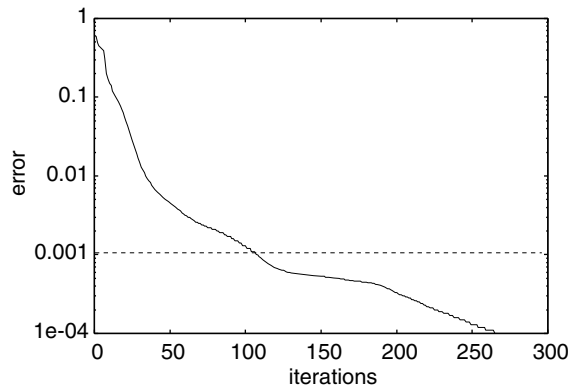| FGMRES tolerance	Number of iterations	Elapse time (s)	Error (%)	
			j	*m*
10^{-3}	108	7771	0.624	1.52
10^{-4}	267	18,409	0.355	0.161

Fig. 10. Mode of convergence of FGMRES.

5.2. Scattering by two-dimensional array of dielectric spheres

5.2.1. Single layer of spheres (normal incidence)

We next consider the scattering by two-dimensional array of dielectric spheres shown in Fig. 11. This example is intended as a model of the so called slab photonic crystals.

In this example the spheres are arranged in one layer and the incident angle is perpendicular to this layer. The unit cell is as shown in Fig. 12. The radius of the dielectric sphere is $D = 0.7L$ and the relative permittivity of the dielectric sphere is $\epsilon^{\mathrm{sph}}/\epsilon^{\mathrm{vacuum}} = (1.6)^2$. The surface of the sphere is divided into 5120 planar triangular elements. Hence the total degrees of freedom are 15,360.
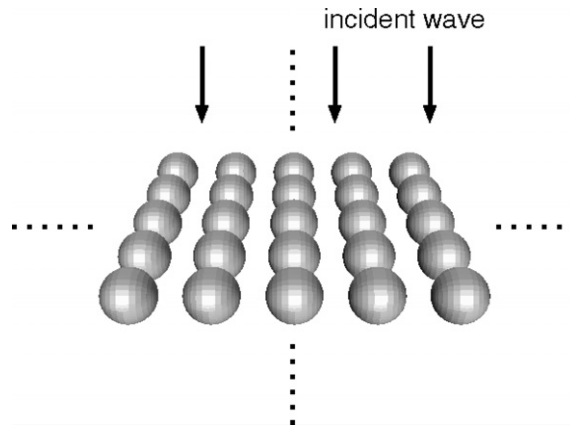
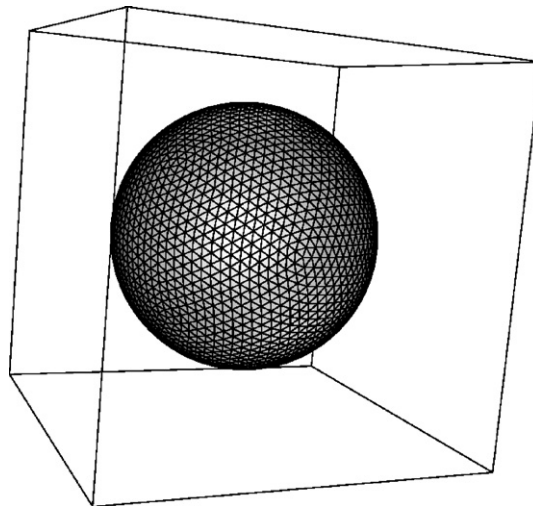Fig. 11. Two-dimensional array of spherical dielectric spheres (normal incidence).

Fig. 12. Unit cell (normal incidence).

For this model we have computed the energy reflectance in the frequency range of $kL = 1.5$–10. The computed energy reflectance is presented in Fig. 13. The solid line in Fig. 13 indicates the results by Stefanou and Modinos [20], while the results shown by $\times$ are those obtained by the present formulation. Again, the agreement is satisfactory.

This analysis, carried out with 8CPUs, took 4–18 min of elapsed time for one wavelength.

5.2.2. Single layer of spheres (oblique incidence)

We next consider the scattering of an obliquely incident electromagnetic waves by a single layer of dielectric spheres shown in Fig. 14. The incident angle is $30°$ and the direction of the polarisation is that $\boldsymbol{E}^{\mathrm{inc}}$ is inclined by $30°$ from the x_2–x_3 plane (where the spheres are) while $\boldsymbol{H}^{\mathrm{inc}}$ is parallel to the x_2–x_3 plane as indicated in Fig. 14.

In this example the dielectric spheres are more densely packed than in the previous model, as one can see in Fig. 15. The radius of the sphere is $D = 0.99L$ and the distance between neighbouring spheres is very small. The sphere is divided into 8000 planar triangular elements and the total degrees of freedom are 24,000. The relative dielectric constant of the spheres is 8.67.
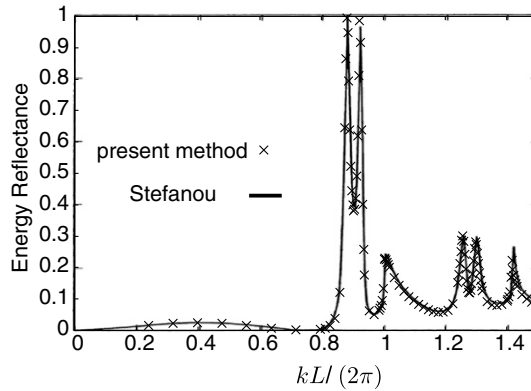
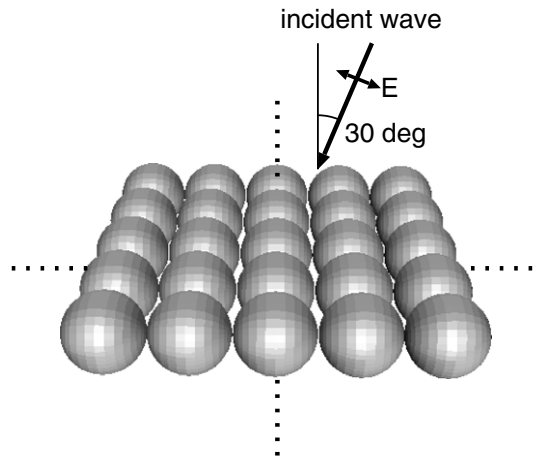Fig. 13. Energy reflectance (normal incidence).

Fig. 14. Two-dimensional array of dielectric spheres (oblique incidence).

The energy transmittance for the range of the wave number given by $kL = 2.635$–4.024 has been computed and plotted in Fig. 16. The solid lines in Fig. 16 indicate the results obtained by Ohtaka et al. [21], while $\times$ indicate the results obtained with the present formulation.

Ohtaka et al. considers the case with $D = L$, i.e. the case where the spheres are in contact, which is not identical with the case considered here. As is expected from this difference the results obtained with the present formulation is slightly different from Ohtaka's results. Indeed, they differ near $kL = 3.5$ and the locations of the spikes are slightly different in $kL = 3.6$–3.8. Otherwise the agreement is satisfactory.

5.2.3. Woodpile crystals

Finally, we consider models of woodpile crystals. The first model we deal with in this section consists of five layers of woodpiles (height: 200 nm, width: 180 nm) made of silicon (optical index: 3.45) which sit on a thin silicon nitride layer whose thickness is 70 nm (optical index: 2). The distance between the centres of the woodpiles in the directions of x_2 and x_3, denoted by $d_{1,1}$, is 650 nm. The media above and below the structure are air and silicon, respectively. The structure is subjected to a plane incident wave whose incident angle is 20° and whose $\boldsymbol{E}$ component is within the incident plane. See Fig. 17 for the x_1–x_2 and x_1–x_3 cross-sections of the model. (The x_1 axis is taken downward from the air side into the silicon base side for technical reasons.) This model has been considered by Gralak et al. [22] in their investigation of photonic band gaps in woodpile crystals.
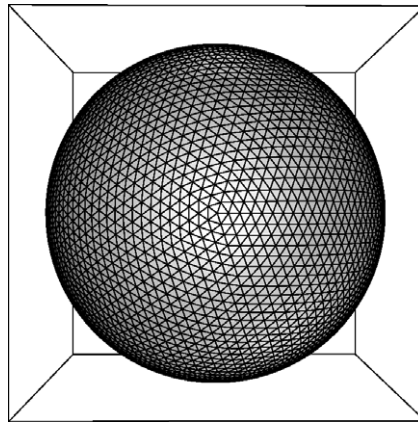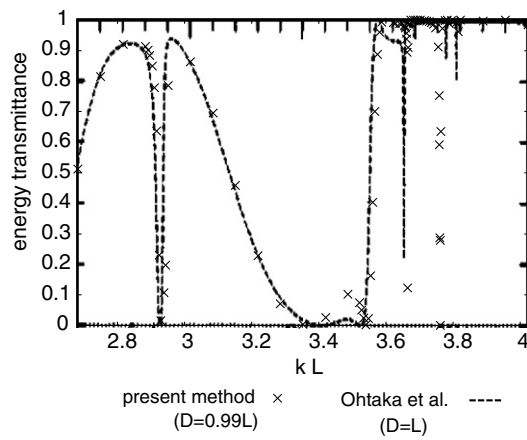
Fig. 15. Unit cell (oblique incidence).

present method ×
(D=0.99L)

Ohtaka et al. - - - -
(D=L)

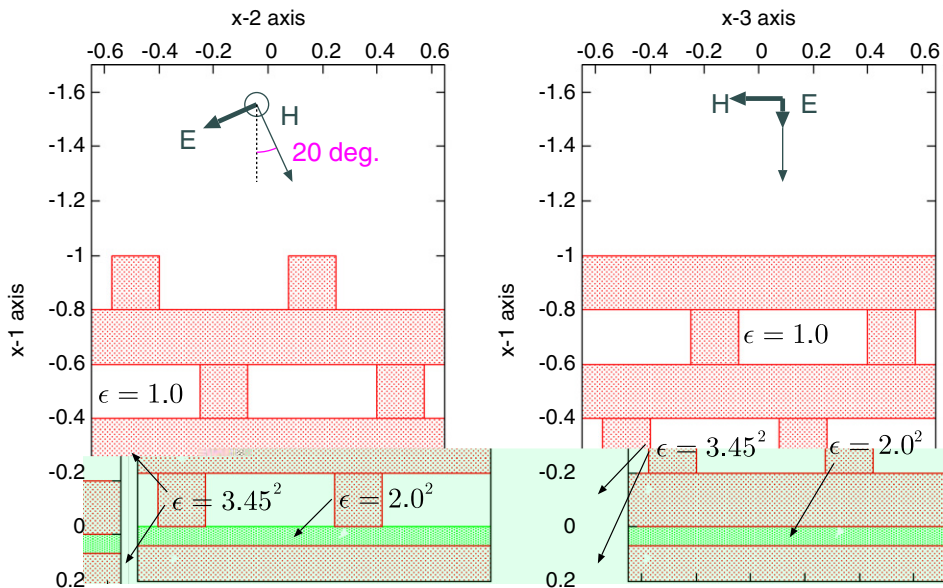Fig. 16. Energy transmittance (oblique incidence).

Fig. 17. x_1–x_2 and x_1–x_3 cross-sections of the woodpile crystal. Unit of length: μm.
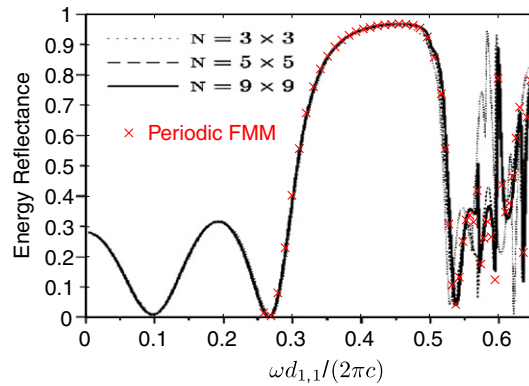
Fig. 18. Reflectance of the woodpile crystal.

In our investigation we have chosen two spatial periods (in $x_{2,3}$ directions) of the structure as the unit cell. The mesh we have used includes 28,800 elements with 43,104 edges. Hence the total number of unknowns is 86,208.

We have computed the energy reflectances of this structure for a range of wave numbers and compared the results obtained with the present method with those reported by Gralak et al. [22]. As seen in Fig. 18, our results agreed well with the most accurate results, denoted by '$N = 9 \times 9$', obtained by Gralak et al.

We next considered a similar model where we have eight layers of woodpiles instead of five. Also, parts of woodpiles in the fourth and fifth layers are removed. See Fig. 19 for the precise geometry of the model. This problem is chosen purely for the purpose of analysis and is not intended as a model of realistic structures. We note that the method by Gralak et al. [22] cannot be applied to this problem since their method is for structures whose material property varies only unidirectionally at a depth in a layer. As is shown in Fig. 19, we divide the domain into two parts by using a virtual boundary at $x_1 = -0.8$. This is because we cannot take one cubic unit cell for this model since the height of the woodpile structure in the x_1 direction is larger than
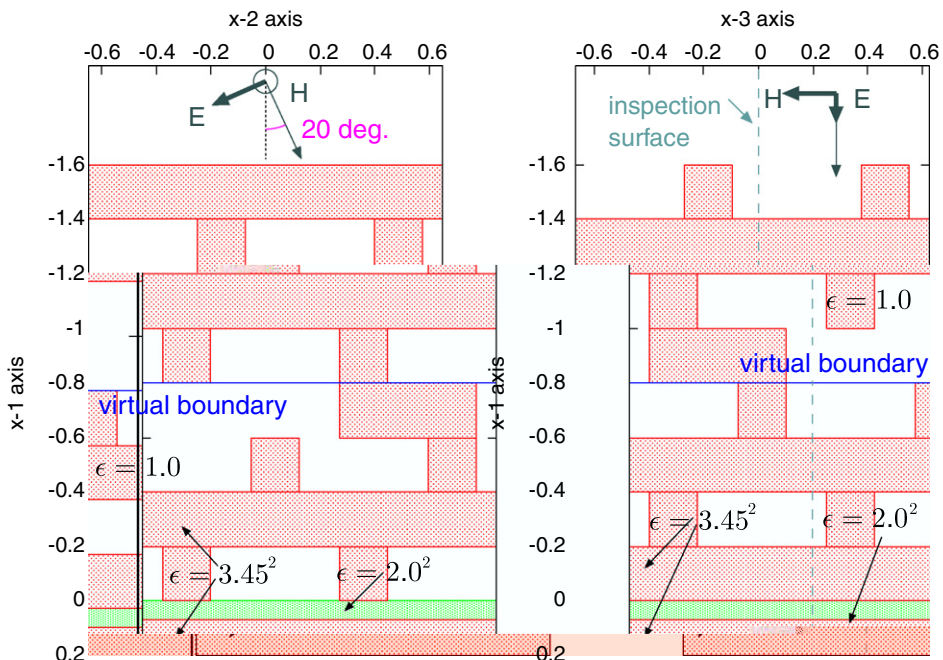

Fig. 19. x_1–x_2 and x_1–x_3 cross-sections of the woodpile crystal with cuts.
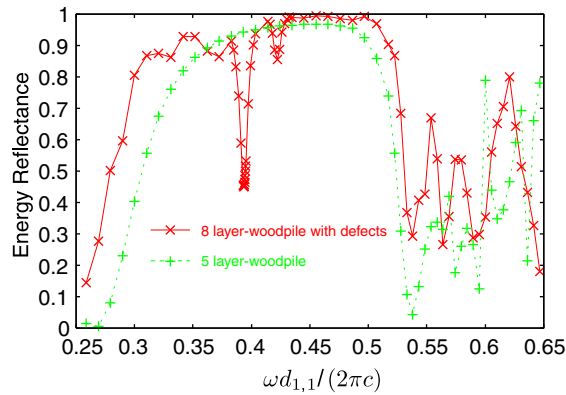
Fig. 20. Reflectance of the woodpile crystal with cuts.

the spatial period. As has been stated, however, this limitation is not essential and can be removed without difficulty. The mesh used for this model includes 40,608 surface elements and 60,720 edges. Hence the total number of unknowns is 121,440.

We have computed the energy reflectances of this structure for a range of wave numbers and plotted the results in Fig. 20 together with the perfect woodpile results computed in the previous example. A sharp passband is seen near $\omega d_{1,1}/(2\pi c) \approx 0.3935$.

To understand the mechanism of this passband, we have plotted the magnitudes (in log scale) of the real part of the Poynting vector defined by $\boldsymbol{S} = \frac{1}{2}(\boldsymbol{E} \times \overline{\boldsymbol{H}})$, on a plane within the structure, whose precise location is indicated by 'inspection surface' in Fig. 19. Fig. 21 shows the magnitudes of the real part of the Poynting vector at $\omega d_{1,1}/(2\pi c) \approx 0.3935$ where the reflectance takes the minimum value, and at $\omega d_{1,1}/(2\pi c) \approx 0.4035$ which is outside the passband. This figure clearly shows that a localised mode exists at $\omega d_{1,1}/(2\pi c) \approx 0.3935$.

The inversion in the process of preconditioning is carried out approximately using GMRES, which we terminate after 30 iterations or when the norm of the error is less than 10^{-1} times its initial value. The maximum CPU time for one analysis for one wave number was about 4H 44M in this example.
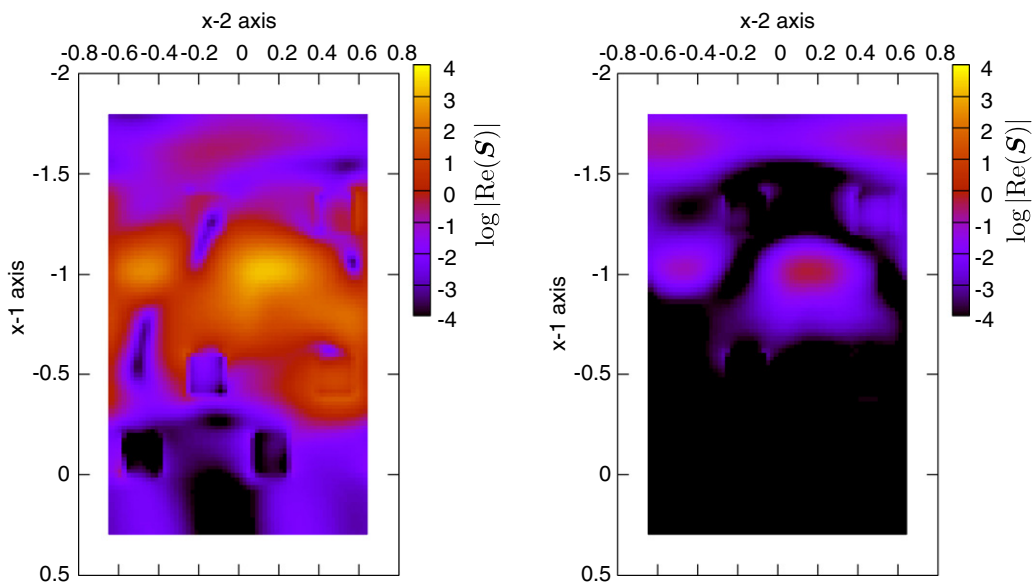

Fig. 21. Magnitudes of the time averaged Poynting vector at $\omega d_{1,1}/(2\pi c) \approx 0.3935$ (left) and at $\omega d_{1,1}/(2\pi c) \approx 0.4035$ (right).

6. Concluding remarks

(1) In this paper we presented an FMM for periodic boundary value problems for Maxwell's equations in 3D. With the periodic Green's function we could derive a periodised M2L formula, which enabled us to solve periodic boundary value problems in the format of the ordinary FMM. The lattice sums included in the periodised M2L formula were converted into Fourier integrals and evaluated accurately. We could verify the proposed method by comparing the obtained numerical results with analytic solutions or with numerical solutions from previous studies.

The problems considered include scattering by dielectric spheres and woodpile structures, both of which are standard and important models in the field of photonic crystals. In the case of woodpile structures, we could find a passband related to a localised mode. Through these numerical tests we could confirm the efficiency and accuracy of the present method. These results indicate that the present method has a potential as a tool for numerical analysis in the field of photonic crystals. In the future work we plan to extend the applicability of the proposed method to more challenging problems including larger and more realistic problems and metamaterial applications.

(2) In scattering problems for periodic structures, one may possibly have guided waves which propagate in the directions of periodicity at certain wave numbers. One may also have leaky guided waves which are known to cause large variations of the solutions for a very small change in wave numbers. The latter phenomenon is known as Wood's anomaly [23]. Generally speaking, the accuracy of numerical results may become worse when Wood's anomaly occurs. Our experience tells, however, that we can avoid this problem of degraded accuracy just by using fine meshes. Further discussions on these issues will be presented elsewhere.

Acknowledgment

Appendix. Evaluation of lattice sums

In this appendix we present our method of evaluating the lattice sum given by $\sum_{\omega \in \mathcal{L}'} O_n^m(-\omega)$.

To start with we note that the following recursive relations for O_n^m hold:

$$O_{n+1}^m = \frac{1}{\sqrt{(n+m+1)(n-m+1)}} \left(\sqrt{(n-m)(n+m)} O_{n-1}^m - \frac{2n+1}{k} \frac{\partial}{\partial x_3} O_n^m \right),$$

$$O_{n+1}^{m+1} = \frac{1}{\sqrt{(n+m+1)(n+m+2)}} \left(-\sqrt{(n-m)(n-m-1)} O_{n-1}^{m+1} - \frac{2n+1}{k} 2\frac{\partial}{\partial \bar{z}} O_n^m \right),$$

where $2\frac{\partial}{\partial \bar{z}} = \frac{\partial}{\partial x_1} + \mathrm{i}\frac{\partial}{\partial x_2}$. We can thus reduce the evaluation of $\sum_{\omega \in \mathcal{L}'} O_n^m(-\omega)$ to that of

$$S_{lm} = \sum_{\omega \in \mathcal{L}'} \left(L\frac{\partial}{\partial x_3} \right)^l \left(2L\frac{\partial}{\partial \bar{z}} \right)^m O_0^0(\boldsymbol{x} - \boldsymbol{\omega}) \mathrm{e}^{\mathrm{i}\boldsymbol{\beta} \cdot \boldsymbol{\omega}} \Bigg|_{\boldsymbol{x}=0}.$$

We now divide the set $\mathcal{L}'$ into four subgroups denoted by $\mathcal{L}_i'$ ($i = 1, \ldots, 4$) (see Fig. 22) and defined as follows:

$$\mathcal{L}_1' = \{(0, \omega_2, \omega_3) |\ \omega_2 = pL,\ \omega_3 = qL,\ p, q \in \mathbb{Z},\ a \leqslant |p|\},$$
$$\mathcal{L}_2' = \{(0, \omega_2, \omega_3) |\ \omega_2 = pL,\ \omega_3 = qL,\ p, q \in \mathbb{Z},\ 2 \leqslant |p| \leqslant a-1\},$$
$$\mathcal{L}_3' = \{(0, \omega_2, \omega_3) |\ \omega_2 = 0,\ \omega_3 = qL,\ q \in \mathbb{Z},\ 2 \leqslant |q|\},$$
$$\mathcal{L}_4' = \{(0, \omega_2, \omega_3) |\ \omega_2 = \pm L,\ \omega_3 = qL,\ q \in \mathbb{Z},\ 2 \leqslant |q|\},$$

where $a > 2$ is a natural number. Correspondingly, the sum S_{lm} is decomposed into the contributions from these sets. Namely,
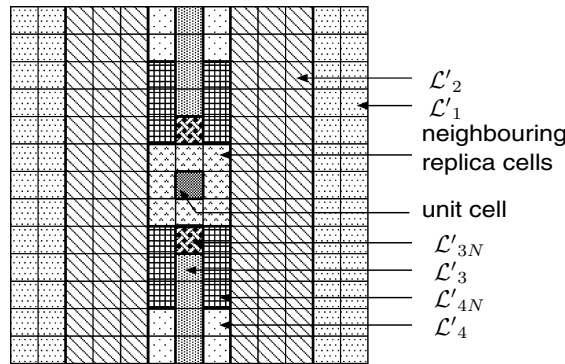
Fig. 22. Grouping of the replica cells.

$$S_{lm} = S_{lm}^1 + S_{lm}^2 + S_{lm}^3 + S_{lm}^4,$$

where S_{lm}^i are defined by

$$S_{lm}^i = \sum_{\boldsymbol{\omega} \in \mathcal{L}_i'} \left(L \frac{\partial}{\partial x_3} \right)^l \left(2L \frac{\partial}{\partial \bar{z}} \right)^m O_0^0(\boldsymbol{x} - \boldsymbol{\omega}) \mathrm{e}^{\mathrm{i}\boldsymbol{\beta}\cdot\boldsymbol{\omega}} \bigg|_{\boldsymbol{x}=0}.$$

We now evaluate the numbers S_{lm}^i after converting them into Fourier integrals as in the 2D case [7]. We here list the results only:

$$S_{lm}^1 = \frac{\mathrm{i}^{l+m-1}}{kL} \sum_{j=\infty}^{\infty} \xi_3^l \left(\int_{-\infty}^{\infty} (\xi_1 + p)^m \frac{\mathrm{e}^{a(\mathrm{i}\beta_2 - p)}}{p(1 - \mathrm{e}^{\mathrm{i}\beta_2 - p})} \, \mathrm{d}\xi_1 + \int_{-\infty}^{\infty} (\xi_1 - p)^m \frac{\mathrm{e}^{a(-\mathrm{i}\beta_2 - p)}}{p(1 - \mathrm{e}^{-\mathrm{i}\beta_2 - p})} \, \mathrm{d}\xi_1 \right),$$

where we have $p = \sqrt{\xi_1^2 + \xi_3^2 - (kL)^2}$, $\xi_3 = 2j\pi + \beta_3$.

$$S_{ml}^2 = \mathrm{i}^{l+m} \frac{\pi}{kL} \sum_{\omega_2 = pL, \; 2 \leqslant p \leqslant a-1} \left(\mathrm{e}^{\mathrm{i}\beta_2\omega_2} + (-1)^m \mathrm{e}^{-\mathrm{i}\beta_2\omega_2} \right) \sum_{j=-\infty}^{\infty} \xi_3^l \left(\sqrt{(kL)^2 - \xi_3^2} \right)^m H_m^{(1)} \left(\sqrt{(kL)^2 - \xi_3^2} \, \omega_2 \right),$$

where $\xi_3 = 2j\pi + \beta_3$ and $H_m^{(1)}$ is the Hankel function of the 1st kind and mth order.

$$S_{ml}^3 = \delta_{m0} \frac{1}{\mathrm{i}kL} \left(\mathrm{e}^{\mathrm{i}b\beta_3} \int_0^\infty \frac{\sqrt{r^2 - (kL)^2}^{\,l-1} \mathrm{e}^{-b\sqrt{r^2 - (kL)^2}}}{1 - \mathrm{e}^{\mathrm{i}\beta_3 - \sqrt{r^2 - (kL)^2}}} r \, \mathrm{d}r + (-1)^l \mathrm{e}^{-\mathrm{i}b\beta_3} \int_0^\infty \frac{\sqrt{r^2 - (kL)^2}^{\,l-1} \mathrm{e}^{-b\sqrt{r^2 - (kL)^2}}}{1 - \mathrm{e}^{-\mathrm{i}\beta_3 - \sqrt{r^2 - (kL)^2}}} r \, \mathrm{d}r \right)$$
$$+ \sum_{\boldsymbol{\omega} \in \mathcal{L}_{3N}'} \left(L \frac{\partial}{\partial x_3} \right)^l \left(2L \frac{\partial}{\partial \bar{z}} \right)^m O_0^0(\boldsymbol{x} - \boldsymbol{\omega}) \mathrm{e}^{\mathrm{i}\boldsymbol{\beta}\cdot\boldsymbol{\omega}} \bigg|_{\boldsymbol{x}=0}, \tag{41}$$

where $\mathcal{L}_{3N}'$ is the set defined by

$$\mathcal{L}_{3N}' = \{ (0, \omega_2, \omega_3) | \; \omega_2 = 0, \; \omega_3 = qL, \; q \in \mathbb{Z}, \; 2 \leqslant |q| \leqslant b-1 \}$$

and $b > 2$ is a natural number.

$$S_{lm}^4 = \frac{\mathrm{i}^{m-1}}{kL} \left(\mathrm{e}^{\mathrm{i}\beta_2} + (-1)^m \mathrm{e}^{-\mathrm{i}\beta_2} \right) \left(\mathrm{e}^{\mathrm{i}c\beta_3} \int_0^\infty \frac{\sqrt{r^2 - (kL)^2}^{\,l-1} \mathrm{e}^{-c\sqrt{r^2 - (kL)^2}}}{1 - \mathrm{e}^{\mathrm{i}\beta_3 - \sqrt{r^2 - (kL)^2}}} r^{m+1} J_m(r) \, \mathrm{d}r \right.$$
$$\left. + (-1)^l \mathrm{e}^{-\mathrm{i}c\beta_3} \int_0^\infty \frac{\sqrt{r^2 - (kL)^2}^{\,l-1} \mathrm{e}^{-c\sqrt{r^2 - (kL)^2}}}{1 - \mathrm{e}^{-\mathrm{i}\beta_3 - \sqrt{r^2 - (kL)^2}}} r^{m+1} J_m(r) \, \mathrm{d}r \right) + \sum_{\boldsymbol{\omega} \in \mathcal{L}_{4N}'} \left(L \frac{\partial}{\partial x_3} \right)^l \left(2L \frac{\partial}{\partial \bar{z}} \right)^m O_0^0(\boldsymbol{x} - \boldsymbol{\omega}) \mathrm{e}^{\mathrm{i}\boldsymbol{\beta}\cdot\boldsymbol{\omega}} \bigg|_{\boldsymbol{x}=0},$$

where

$$\mathcal{L}'_{4N} = \{(0, \omega_2, \omega_3) |\ \omega_2 = \pm L,\ \omega_3 = qL,\ q \in \mathbb{Z},\ 2 \leqslant |q| \leqslant c - 1\},$$

$c > 2$ is a natural number and J_m is the Bessel function of the mth order. We evaluate the integrals in S^1_{lm}, S^3_{lm} and S^4_{lm} numerically using the steepest descent paths for the exponentials in the integrand as the paths of integration. One can increase the (integer) parameters a, b and c for accelerating the convergence of these integrals, but one can do so at the cost of increased computational load for evaluating direct sums. In the present investigation we have set $a = b = c = 100$.

References

[1] J.D. Joannopoulos, R.D. Meade, J.N. Winn, Photonic Crystals, Princeton University Press, 1995.
[2] J.B. Pendry, Negative refraction makes a perfect lens, Phys. Rev. Lett. 85 (2000) 3966–3969.
[3] L. Greengard, V. Rokhlin, A fast algorithm for particle simulations, J. Comput. Phys. 73 (1987) 325–348.
[4] N. Nishimura, Fast multipole accelerated boundary integral equation methods, Appl. Mech. Rev. 55 (2002) 299–324.
[5] Y. Otani, N. Nishimura, An FMM for periodic elastostatic crack problems in 2D, Trans. JASCOME J. BEM 21 (2004) 71–76 (in Japanese).
[6] Y. Otani, N. Nishimura, A fast multipole boundary integral equation method for periodic boundary value problems in three dimensional elastostatics and its application to homogenisation, Int. J. Multiscale Comput. Eng. 4 (2006) 487–500.
[7] Y. Otani, N. Nishimura, An FMM for periodic boundary value problems for cracks for Helmholtz' equation in 2D, Int. J. Numer. Meth. Eng. 73 (2008) 381–406.
[8] M.S. Yeung, E. Barouch, Three-dimensional nonplanar lithography simulation using a periodic fast multipole method, Proc. SPIE 3051 (1997) 509–521.
[9] J.-C. Nédélec, Acoustic and Electromagnetic Equations, Springer, 2001.
[10] W.C. Chew, J.-M. Jin, E. Michielssen, J. Song (Eds.), Fast and Efficient Algorithms in Computational Electromagnetics, Artech House, 2001.
[11] V. Rokhlin, Rapid solution of integral equations of scattering theory in two dimensions, J. Comput. Phys. 86 (1990) 414–439.
[12] Y. Otani, N. Nishimura, On the improvement and preconditioning for FMM for Helmholtz' equation in 2D, J. Appl. Mech., JSCE 6 (2003) 283–292 (in Japanese).
[13] L.J. Jiang, W.C. Chew, A mixed-form fast multipole algorithm, IEEE Trans. Antennas Propag. 53 (2005) 4145–4156.
[14] H. Cheng, W.Y. Crutchfield, Z. Gimbutas, L.F. Greengard, J.F. Ethridge, J. Huang, V. Rokhlin, N. Yarvin, J. Zhao, A wideband fast multipole method for the Helmholtz equation in three dimensions, J. Comput. Phys. 216 (2006) 300–325.
[15] L.C. Biedenharn, J.D. Louck, P.A. Carruthers, Angular Momentum in Quantum Physics, Addison-Wesley, 1981.
[16] N.A. Gumerov, R. Duraiswami, Fast Multipole Methods for the Helmholtz Equation in Three Dimensions, Elsevier, 2005.
[17] S. Enoch, R.C. McPhedran, N.A. Nicorovici, L.C. Botten, J.N. Nixon, Sums of spherical waves for lattices layers and lines, J. Math. Phys. 42 (2001) 5859–5870.
[18] Y. Saad, Iterative Methods for Sparse Linear Systems, second ed., SIAM, 2003.
[19] S.M. Rao, D.R. Wilton, A.W. Glisson, Electromagnetic scattering by surfaces of arbitrary shape, IEEE Trans. Antennas Propag. AP-30 (1982) 409–418.
[20] N. Stefanou, A. Modinos, Scattering of light from a two-dimensional array of spherical particles on a substrate, J. Phys. Cond. Matt. 3 (1991) 8135–8148.
[21] K. Ohtaka, Y. Suda, S. Nagano, T. Ueta, A. Imada, T. Koba, J.S. Bae, K. Mizuno, S. Yano, Y. Segawa, Photonic band effects in a two-dimensional array of dielectric spheres in the millimeter-wave region, Phys. Rev. B 61 (2000) 5267–5279.
[22] B. Gralak, M. de Dood, G. Tayeb, S. Enoch, D. Mastre, Theoretical study of photonic band gaps in woodpile crystals, Phys. Rev. E 67 (2003) 066601.
[23] R. Petit (Ed.), Electromagnetic Theory of Gratings, Springer-Verlag, 1980.